First Observation of Cross-Beam Energy Transfer Mitigation for Direct-Drive Inertial Confinement Fusion Implosions Using Wavelength Detuning at the National Ignition Facility

In direct-drive inertial confinement fusion (ICF), laser beams irradiate a plastic shell containing a thick layer of frozen deuterium–tritium (DT) and ablatively drive an implosion. The ultimate goal of ICF is ignition and energy gain; the minimum shell kinetic energy required for ignition (defined as when the energy from DT fusion reactions exceed the laser energy incident on the target) is given by $E_{\min} \sim \alpha^{1.88} P_{\mathrm{abl}}^{-0.77} v_{\mathrm{imp}}^{-5.89}$ (Ref. 1), where the three parameters of the implosion—α, v_{imp}, and P_{abl} [adiabat (the ratio of the fuel pressure to the Fermi-degenerate pressure at peak implosion velocity), implosion velocity, and ablation pressure, respectively]—are determined primarily by the deposition of the laser energy into the coronal plasma of the target, the subsequent heat conduction to the ablation surface, and the resulting equation of state (EOS) of the shell material. Cross-beam energy transfer (CBET)[2] has been identified in direct-drive experiments on the OMEGA[3] and National Ignition Facility (NIF)[4] lasers to significantly reduce absorption, ablation pressure, and implosion velocity.

The role of CBET in direct drive was identified in early research[5,6] but only recently identified as the leading cause of decreased energy coupling. When attempts were made to match multiple calculated observables (shell morphology, trajectory, scattered-light spectra and distribution, and shock timing) with experiments, the critical role of CBET became apparent:[7,8] lowering laser absorption by 20% to 30%. Good agreement with the multiple experimental observables was obtained[7,8] when both the CBET and nonlocal electron transport[9] models were included in 1-D *LILAC*[10] and 2-D *DRACO*[11] simulations. Historically, the role of CBET[5,6] was masked by using a flux-limited electron transport model that matched laser absorption.

CBET laser–plasma interaction results from two-beam energy exchange via stimulated Brillouin scattering (SBS),[2] which reduces absorbed light and consequently reduces ablation pressure and implosion velocity. The dominant CBET loss mechanism in direct drive occurs when rays counter-propagate (backscatter mode), thereby increasing scattered light, as illustrated in Fig. 152.1(a). For the ignition-relevant overlapped beam intensities of $\sim 8 \times 10^{14}$ W/cm^2 for these NIF experiments, CBET is calculated to reduce laser absorption by 22%, the average implosion speed by ~9%, and the average ablation pressure by 35% via simulations of the experimental

(a)

Blue-shifted probe

Pump beam

Red-shifted probe

CBET extracts energy from the pump to the probe ray

Target r_c

Refractive shadow boundary

Probe beam

(b)
DRACO CBET simulation

NIF PDD
N160406
7 ns

CBET gain ($\times 10^{15}$ W/cm^3)
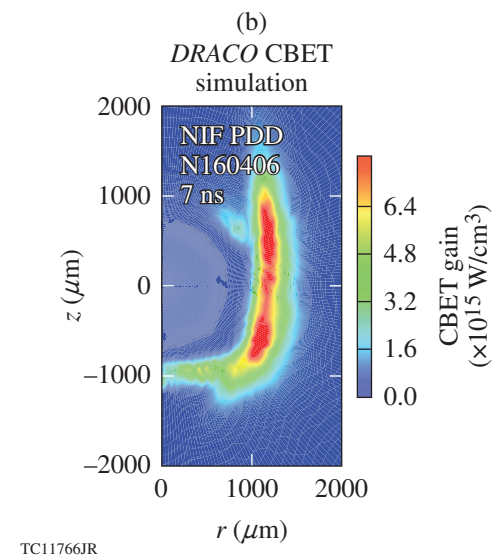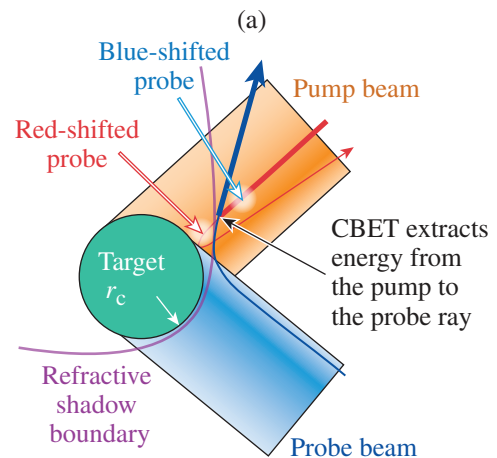
TC11766JR

Figure 152.1

(a) The effect of cross-beam energy transfer (CBET) in polar direct drive (PDD) predominantly affects the equatorial region; (b) successful CBET mitigation benefits the same region.

conditions. These drive-related results are consistent with other ongoing OMEGA-[7] and NIF-scale[8] experiments. Reducing the target mass compensates for CBET losses, but the thinner shells become compromised as a result of instability growth.[12] As shown by the above equation for E_{min}, efficient laser energy coupling and hydrodynamic stability are essential aspects of direct-drive ICF, making CBET mitigation vital. Mitigation strategies of the deleterious CBET effects invoke combinations of spatial, temporal, and wavelength domains. Wavelength detuning, the focus of this article, works by altering the resonance condition between interacting beams.[2] Wavelength detuning was first examined for indirect drive[13] and subsequently for direct drive but was prematurely dismissed as a viable option.[14]

The first direct-drive experiments have been designed for the NIF to study the efficacy of wavelength-detuning CBET mitigation. The target designed for these wavelength-detuning shots on the NIF was adapted from existing 600-kJ designs,[8] where the trajectories and the shape of the imploding shell and scattered light were well described by the CBET model in *DRACO*. The basic target design is shown as the inset in Fig. 152.2, where the laser beam power (shown in red) produces a peak overlapped intensity of $\sim 8 \times 10^{14}$ W/cm^2 at the initial target radius.
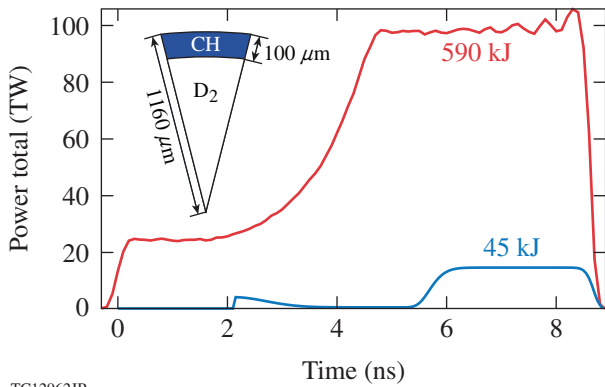

TC12962JR

Figure 152.2

The NIF PDD target design for wavelength detuning with cone swapping to induce a wavelength difference across the equator. The total 590-kJ design pulse is shown in red; the 45-kJ backlighter pulse is shown in blue. Inset: the warm plastic (CH), 1160-μm-radius, 100-μm-thick shell with a 20-atm D$_2$ gas fill.

The indirect-drive NIF beam geometry distributes 192 beam ports [grouped into 48 quads, shown as projected circles in Fig. 152.3(a)] toward the poles of the NIF target chamber, forming cones of quads with a common polar angle.[15] Repoint-

ing higher-intensity beams from lower latitudes toward the equator partially compensates for the NIF port geometry and higher incident angles when illuminating direct-drive targets. In this modified configuration, referred to as polar direct drive (PDD),[16,17] CBET predictably dominates in the equatorial region where most of the crossing-beam interactions occur,[18,19] as shown in Fig. 152.1(b). As a result, PDD implosions tend to become oblate because CBET reduces the laser drive preferentially in the equatorial region. With this motivation, a basic wavelength-detuning strategy exploits the PDD configuration, where each hemisphere has a different wavelength or color. However, the nominal symmetric wavelength mapping [see Fig. 152.3(a)] developed for indirect-drive targets precludes achieving hemispheric wavelength detuning using typical PDD repointing configurations.[17]
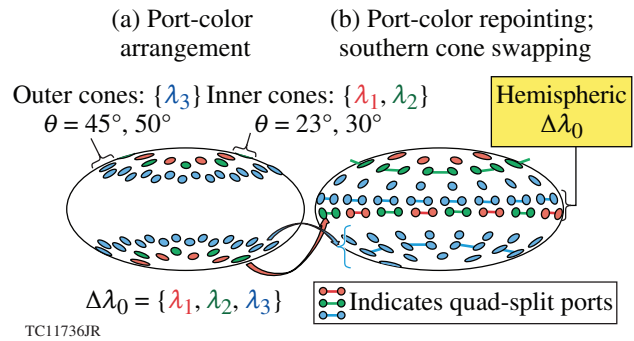

TC11736JR

Figure 152.3

NIF Quad-Port Hammer projections for the wavelength-detuning CBET mitigation scheme. (a) Indirect-drive mapping where the colored symbols indicate relative wavelength; (b) PDD repoint mapping that achieves hemispheric detuning, typical northern-hemisphere repointing, and southern-hemisphere cone swapping.

The NIF fiber front end[15] supports three separate initial colors or wavelength shifts $\Delta\lambda_0 = \{\lambda_1, \lambda_2, \lambda_3\}$ detuned from a central wavelength $\lambda_0 \sim 351$ nm. Currently, the three-color $\{\lambda_1, \lambda_2, \lambda_3\}$ mapping onto the NIF indirect-drive ports is symmetric about the equator [see Fig. 152.3(a)]. To induce a wavelength difference about the equatorial region, a dramatic repointing (referred to as "cone swapping") is required in either the northern or southern hemisphere [see Fig. 152.3(b) for the southern case]. For cone swapping, in one hemisphere the higher-latitude ports ("inner cones": $\{\lambda_1, \lambda_2\}$) are repointed to the equator and the lower-latitude ports ("outer cones": $\{\lambda_3\}$) are repointed to the mid- and high latitudes. For the wavelength-detuning experiments described here, only two different colors were specified such that $\lambda_1 = \lambda_2 \neq \lambda_3$, although future enhanced experiments with three colors are planned. The current NIF

configuration, while not optimal, is capable of achieving a modest wavelength-detuning level $\Delta\lambda_0 = \{+2.3, +2.3, -2.3\}$ Å UV, which is adequate for these proof-of-principle experiments. Cone swapping plus wavelength detuning induces the desired partial hemispheric wavelength difference between beams crossing the equatorial region.

The far-field spot envelope [induced from distributed phase plates (DPP's)[20] and small-divergence smoothing] quad-mapping is given by the current indirect-drive configuration on the NIF: the inner cones (λ_1, λ_2; red/green projected circles in Fig. 152.3) use a wide elliptical spot shape not well suited for the equatorial region, while the outer cones (λ_3; blue projected circles in Fig. 152.3) use a narrow elliptical spot shape. The values of the beam energy and repointing were additionally adjusted in the cone-swapping hemisphere to compensate for the swapped spot shapes and the higher incident angles using established PDD design principles.[17] The cone-swapping repointing scheme and the fixed DPP quad-mapping result in nonoptimal implosion symmetry [see Fig. 152.3(b)]. For this reason, fusion yield and areal density are not metrics for these experiments, which concentrate instead on observables directly related to laser energy absorption: implosion trajectory, shell morphology, and scattered light. Future reconfigurations (optimal DPP's for PDD,[17,20] flexible color mapping, and larger wavelength separation) can relieve these constraints, and simulations predict improved overall fusion performance.

In direct drive, many overlapping beams interact with each other in a complicated tangle of intensity, directions, and wavelengths, depending on the beam-port configuration surrounding the imploding target. In addition, each beam strongly refracts and chirps in the expanding, evolving plasma atmosphere during propagation and then scatters energy spectra in a wide spread of exiting paths. The *DRACO* CBET package (*Adaawam*)[21] is an integral part of the 3-D ray-trace package (*Mazinisin*[22]),[17] which models each beam as a set of adaptively chosen rays to minimize noise. An extension to the plane-wave CBET model[2] adapts the steady-state fluid model to 3-D interacting rays in *Adaawam* by generalizing the wave-vector phase-matching condition. The CBET model[2] includes relevant SBS physics and results in gain/loss for a probe ray interacting with the total pump angular spectrum. *Adaawam* calculates the CBET interaction self-consistently in conjunction with the hydrodynamic evolution of the ICF target (via a split-step technique) and captures the necessary coupled interaction of the dynamic electron density profile, temperature, and plasma-flow velocity that dictates the behavior of CBET, and vice versa, since CBET and the hydrodynamics are strongly coupled. *Adaawam* uses

advanced iterative feedback control to stabilize the CBET tightly coupled many-beam interactions while maintaining energy conservation. This model has been compared to many observables across a range of implosions on OMEGA[23] and the NIF.[7] An experimentally determined CBET-gain multiplier of 1.5 (from unrelated OMEGA shots[23]) that use the first-principles EOS tables was applied to all pre- and post-shot simulations without attempting to fit the NIF shots having similar intensity but different scale lengths and pulse shapes. The CBET gain multiplier of 1.5 that applies across laser systems indicates a predictive ability on the initial wavelength-detuning shot campaign at the tested $\sim 8 \times 10^{14}$ W/cm^2 intensity range.

Maximal CBET occurs in the rapidly expanding coronal plasma where two interacting rays satisfy the ion-acoustic-wave–matching conditions[2,13,14] that account for propagation direction, wavelength, and fluid flow; e.g., a CBET resonance occurs at the Mach-1 surface given a radial plasma flow for directly opposed radially propagating rays of equal wavelength. The instantaneous ray wavelength is given by its initial value and the temporal derivative of the electron density (an extension of the common Doppler shift[24]), which dynamically alters the instantaneous refractive index in space, and thereby the wavelength, and is independent of ray direction. Consequently, the CBET resonance features are altered as the coronal plasma evolves, which directly maps onto a chirped scattered-light measurement that can be employed to help analyze the implosions and laser–plasma interaction physics. A future publication will address the complete set of measurements and modeling.

Wavelength detuning between crossing beams responds differently in indirect- versus direct-drive ICF implosions, depending on the dominant CBET mode. In indirect drive, the sign of small wavelength detuning (<2-Å UV) is used to control the direction of energy transfer between interacting beams by leveraging the CBET resonance for the forward-scatter mode.[13] While this mode occurs in direct drive, it does not increase scattered-light loss because the energy exchanged is spatially shifted and deposited in slightly different regions; however, distortions at small wavelength separations can arise.[19] In contrast, an outbound ray in the dominant backscatter mode in direct drive experiences CBET gain regardless of the wavelength-difference sign or magnitude (for nominal levels) because the ion-acoustic wave's contribution dominates the CBET resonance function.[19] Under atypical conditions, the outbound ray may experience a loss resonance but insignificantly impacts scattered light because the outbound rays typically transport little energy. The ensemble CBET exchange is best described as an interaction volume (a weighted volume that determines

the interaction strength, which depends on path length, intensity, wavelength, electron density, coronal temperature, fluid velocity, etc.) because any high-gain region is equally matched by loss and significant CBET occurs only when the ensemble interaction volume is large. For example, there might be high intensity near a turning point over insignificant path lengths that form an ineffective and small interaction volume with minimal resulting CBET.

The resonant CBET gain region of the outbound rays in the backscatter mode never disappears but rather shifts into a smaller interaction volume because the relative instantaneous wavelength difference changes the ion-acoustic-wave–matching conditions of the interacting rays. The resonance region bifurcates and shifts both farther out in the corona (where the outbound rays have lower intensity and experience higher expanding fluid velocity and lower electron density) and closer inside the corona (where the interaction becomes shielded by the refractive shadow-boundary surface and/or outbound rays that have negligible intensity)[19] [see Fig. 152.1(a)]. A sufficiently large wavelength separation (detuning) significantly reduces CBET exchange for direct drive by decreasing the interaction volume. In contrast, an insufficient wavelength separation can lead to deposition and shell distortion via the forward-scatter mode.[19] The efficacy of wavelength-detuning CBET mitigation diminishes as the plasma expands and the target implodes, which causes the CBET resonance regions to gradually drift into larger interaction volumes during the drive pulse.[19] Larger wavelength-detuning values delay the onset of diminished mitigation. Simulations predict that wavelength-detuning CBET mitigation is effective for both symmetric direct drive (OMEGA) and PDD since the same mechanisms occur in both configurations, although the positive impact is more pronounced for PDD.[19]

With this motivation, for the first time in direct-drive ICF, wavelength-detuning CBET mitigation was demonstrated and shown to improve energy coupling. The NIF PDD wavelength-detuning CBET mitigation campaign shots were performed in three pairs; each pair consisted of one implosion backlit with ~6.7-keV x rays produced from a planar Fe foil target energized by two quads of NIF beams with 45 kJ (see the blue curve in Fig. 152.2) of UV laser energy per beam with an equatorial view of the compressing shell and a second implosion for self-emission images of the compressing target from equatorial and polar views. Additional diagnostics measured both hard x rays produced by energetic electrons arising from the stimulated Raman and possible two-plasmon–decay instabilities. The inferred levels contain at most only a few percent of the incident energy and do not affect the analysis of the laser–target coupling and CBET.[7] The first pair of control shots (N160405 and N160406) with the same wavelength for all the beams (zero detuning) were performed to establish the baseline experimental observables. Next, two pairs of experiments with a detuning mapping of $\Delta\lambda_0 = \{+2.3, +2.3, -2.3\}$ Å UV were performed to evaluate the efficacy of wavelength-detuning CBET mitigation. The zero-detuning and first-detuning shots (N160821-001 and N160821-002) employed southern-hemisphere cone swapping, as illustrated in Fig. 152.3(b). The second-detuning shots (N170102 and N170103) employed northern-hemisphere cone swapping, primarily to observe the expected image inversion and to effectively image the self-emission from the antipodal pole. The repointing (accounting for mirror-image cone swapping) and pulse shapes were nominally identical for all shots where the only intended difference was the wavelength configuration.

The simulated and measured backlit gated x-ray radiographs are analyzed to show shell morphology evolution as well as in-flight shell trajectory, which are used to infer energy coupling. The gated images (gate time ~100 ps) shown in Fig. 152.4 compare the shell morphology for the three backlit shots. The experimental framing-camera images are a composite of several images close in time for this slowly moving target that were cross-correlated and adjusted for magnification to enhance the signal-to-noise ratio; the measurements used a 30-μm pinhole. The *DRACO* simulations post-processed with the x-ray imaging code *Spect3D*[25] with matching pinholes and gates. The first two rows are radiographs of matched post-shot simulations and experimental results for the baseline zero-detuning and wavelength-detuning shots with southern-hemisphere cone swapping. The last row shows radiographs for detuning shots with northern-hemisphere cone swapping. All the backlit radiograph data show remarkable agreement between simulation and experiment, especially the expected trend for the detuning shots. A mere ~2% to 3% additional laser energy is absorbed with detuning, but since this energy is localized to the equatorial coronal volume fraction (~25%), and the deposition is redistributed to increase hydrodynamic efficiency, the result is dramatic as observed with the gated x-ray radiographs.

Most notable was the design prediction and measurement of the equatorial mass accumulation near the equator with active wavelength detuning (bottom two rows in Fig. 152.4). As predicted, the mass accumulation flipped orientation when cone swapping was applied to the opposite hemisphere. The wavelength-detuning design attempted to minimize the $\ell = 2$ Legendre mode while accounting for the spot shapes, point-

ing, and energies in conjunction with the expected increased drive in the equatorial region caused by CBET mitigation. The equatorial mass accumulation is a common feature in PDD designs (and not directly related to CBET mitigation), which is caused by lateral mass flow toward the equator (from primarily oblique incidence) when sufficient equatorial drive is available (e.g., from CBET mitigation) and when using non-optimal spot shapes while achieving a small $\ell = 2$.

The shell trajectory is inferred from the simulated and experimental backlit radiographs by first extracting the outer steepest gradient surface or radii [see Figs. 152.4 and 152.5 (inset)]. The majority of the CBET gain occurs in the equatorial region [Fig. 152.1(b)] and consequently the region expected to benefit from wavelength detuning. Both the surface-area–weighted average of the whole extracted surface and a range restricted to the equatorial region (shown here) demonstrate the

benefit. When the extracted shell surface is restricted to the equatorial region (±30° region about the equator) and plotted as a function of time (see Fig. 152.5), the inferred implosion speed increases as a result of wavelength-detuning CBET mitigation. The equatorial shell speed increases 9% from 144 to 157 μm/ns based on simulation (experimentally a 16% increase from 133 to 154 μm/ns) because wavelength-detuning CBET mitigation deposits 3% additional energy within the small volume over the equator. The enhanced equatorial velocity is consistently observed when comparing the extracted outer shell contours taken from zero detuning and detuning shots in Fig. 152.5 (inset), where the entire surface-area–weighted average implosion speed increases experimentally by 13%.

In conclusion, the first direct-drive wavelength-detuning CBET mitigation experiments on the NIF with a modest wavelength difference between crossing beams confirmed improved
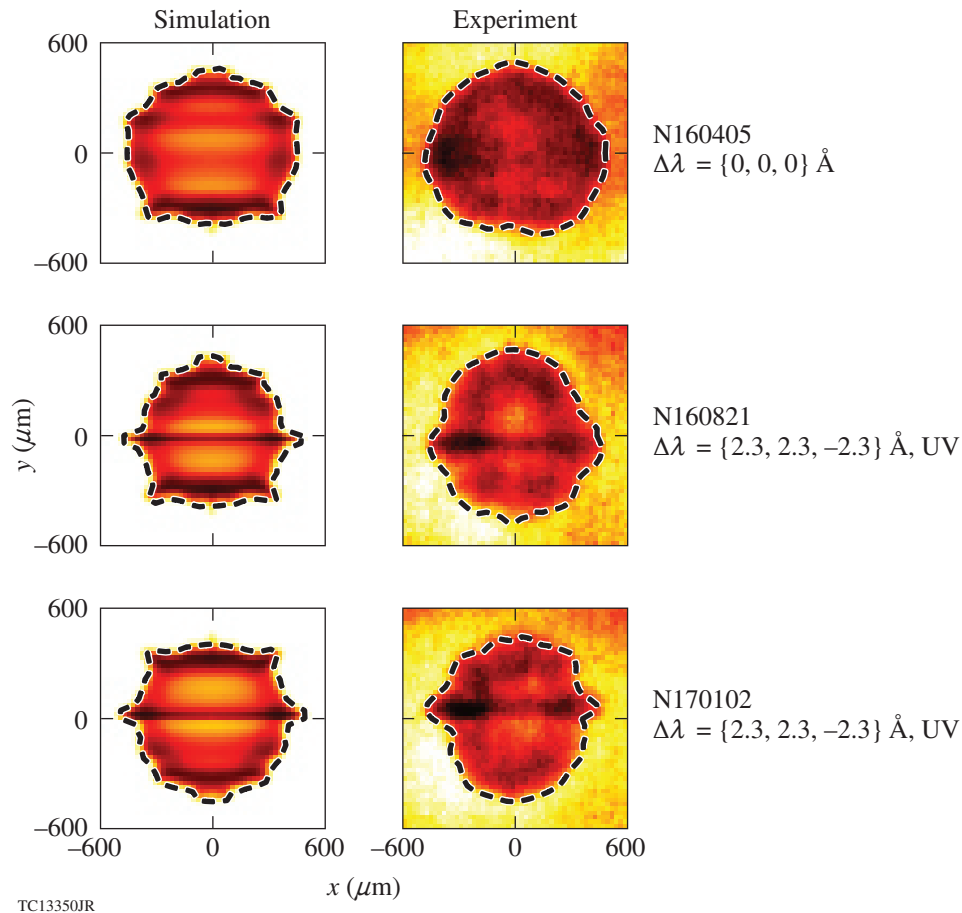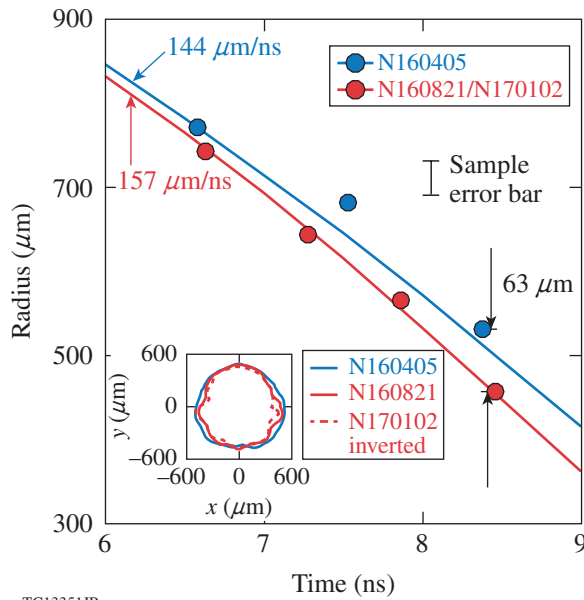

Simulation   Experiment

N160405
$\Delta\lambda = \{0, 0, 0\}$ Å

N160821
$\Delta\lambda = \{2.3, 2.3, -2.3\}$ Å, UV

N170102
$\Delta\lambda = \{2.3, 2.3, -2.3\}$ Å, UV

TC13350JR

Figure 152.4
Comparison of backlit radiographs from post-shot *DRACO* simulations and NIF experimental results near the end of the laser pulse at $t = 8.5$ ns. The dashed lines indicate the outer shell surface extracted from each image defined by the steepest gradient in the inward radial direction.

Figure 152.5
Equatorial shell trajectories from post-processed simulated (solid lines) and experimental (symbols) backlit radiographs. The red lines/symbols represent the baseline zero-detuning experiment (N160405). The blue lines/symbols represent the average of the two detuning experiments (N160821 and N170102). The inset shows superimposed extracted surfaces from the experimental radiographs of Fig. 152.4, exemplifying the equatorial mitigation.

coupling predicted by multidimensional hydrodynamic simulations. These direct-drive proof-of-principle experiments are the first such experiments and provide a path forward to recovering the energy loss caused by CBET. Simulations predict that as the wavelength separation increases (e.g., the ±6-Å UV predicted NIF limit), the equatorial drive continues to improve and requires rebalancing to minimize $\ell = 2$. Simulations also indicate that judicious use of all three colors with flexible color-mapping in the fiber front end on the NIF produces better-balanced CBET mitigation designs in PDD. Simulations predict that symmetric direct drive on OMEGA will benefit from wavelength detuning since its three main driver legs already distribute evenly over the target. Additional CBET mitigation domains may be combined with wavelength detuning, e.g., optimized spot shapes that reduce the laser energy refracting over the horizon while maintaining optimal shape [spot-masking apodization (SMA)[20]]. Future experiments are planned to scope out the capabilities of wavelength-detuning CBET mitigation to further improve coupling and to address the asymmetry by proposing system changes to both OMEGA and the NIF: adding multiple wavelength sources to OMEGA, expanding the NIF's wavelength-detuning range, using SMA-

DPP's, different wavelengths within NIF's quads, and remapping the NIF fiber front end to obviate cone swapping.

ACKNOWLEDGMENT

REFERENCES

1. M. C. Herrmann, M. Tabak, and J. D. Lindl, Nucl. Fusion **41**, 99 (2001).

2. C. J. Randall, J. R. Albritton, and J. J. Thomson, Phys. Fluids **24**, 1474 (1981).

3. T. R. Boehly, D. L. Brown, R. S. Craxton, R. L. Keck, J. P. Knauer, J. H. Kelly, T. J. Kessler, S. A. Kumpan, S. J. Loucks, S. A. Letzring, F. J. Marshall, R. L. McCrory, S. F. B. Morse, W. Seka, J. M. Soures, and C. P. Verdon, Opt. Commun. **133**, 495 (1997).

4. E. M. Campbell and W. J. Hogan, Plasma Phys. Control. Fusion **41**, B39 (1999).

5. C. J. McKinstrie, J. S. Li, R. E. Giacone, and H. X. Vu, Phys. Plasmas **3**, 2686 (1996).

6. C. J. McKinstrie *et al.*, Phys. Plasmas **5**, 1142 (1998).

7. P. B. Radha, M. Hohenberger, D. H. Edgell, J. A. Marozas, F. J. Marshall, D. T. Michel, M. J. Rosenberg, W. Seka, A. Shvydky, T. R. Boehly, T. J. B. Collins, E. M. Campbell, R. S. Craxton, J. A. Delettrez, S. N. Dixit, J. A. Frenje, D. H. Froula, V. N. Goncharov, S. X. Hu, J. P. Knauer, R. L. McCrory, P. W. McKenty, D. D. Meyerhofer, J. Moody, J. F. Myatt, R. D. Petrasso, S. P. Regan, T. C. Sangster, H. Sio, S. Skupsky, and A. Zylstra, Phys. Plasmas **23**, 056305 (2016).

8. M. Hohenberger, P. B. Radha, J. F. Myatt, S. LePape, J. A. Marozas, F. J. Marshall, D. T. Michel, S. P. Regan, W. Seka, A. Shvydky, T. C. Sangster, J. W. Bates, R. Betti, T. R. Boehly, M. J. Bonino, D. T. Casey, T. J. B. Collins, R. S. Craxton, J. A. Delettrez, D. H. Edgell, R. Epstein, G. Fiksel, P. Fitzsimmons, J. A. Frenje, D. H. Froula, V. N. Goncharov, D. R. Harding, D. H. Kalantar, M. Karasik, T. J. Kessler, J. D. Kilkenny, J. P. Knauer, C. Kurz, M. Lafon, C. K. N. LaFortune, B. J. MacGowan, A. J. Mackinnon, A. G. MacPhee, R. L. McCrory, P. W. McKenty, J. F. Meeker, D. D. Meyerhofer, S. R. Nagel, A. Nikroo, S. Obenschain, R. D. Petrasso, J. E. Ralph, H. G. Rinderknecht, M. J. Rosenberg, A. J. Schmitt, R. J. Wallace, J. Weaver, C. Widmayer, S. Skupsky, A. A. Solodov, C. Stoeckl, B. Yaakobi, and J. D. Zuegel, Phys. Plasmas **22**, 056308 (2015).

9. D. Cao, G. Moses, and J. Delettrez, Phys. Plasmas **22**, 082308 (2015).

10. J. Delettrez, R. Epstein, M. C. Richardson, P. A. Jaanimagi, and B. L. Henke, Phys. Rev. A **36**, 3926 (1987).

11. P. B. Radha, V. N. Goncharov, T. J. B. Collins, J. A. Delettrez, Y. Elbaz, V. Yu. Glebov, R. L. Keck, D. E. Keller, J. P. Knauer, J. A. Marozas, F. J. Marshall, P. W. McKenty, D. D. Meyerhofer, S. P. Regan, T. C. Sangster,

D. Shvarts, S. Skupsky, Y. Srebro, R. P. J. Town, and C. Stoeckl, Phys. Plasmas **12**, 032702 (2005).

12. V. N. Goncharov, T. C. Sangster, R. Betti, T. R. Boehly, M. J. Bonino, T. J. B. Collins, R. S. Craxton, J. A. Delettrez, D. H. Edgell, R. Epstein, R. K. Follet, C. J. Forrest, D. H. Froula, V. Yu. Glebov, D. R. Harding, R. J. Henchen, S. X. Hu, I. V. Igumenshchev, R. Janezic, J. H. Kelly, T. J. Kessler, T. Z. Kosc, S. J. Loucks, J. A. Marozas, F. J. Marshall, A. V. Maximov, R. L. McCrory, P. W. McKenty, D. D. Meyerhofer, D. T. Michel, J. F. Myatt, R. Nora, P. B. Radha, S. P. Regan, W. Seka, W. T. Shmayda, R. W. Short, A. Shvydky, S. Skupsky, C. Stoeckl, B. Yaakobi, J. A. Frenje, M. Gatu-Johnson, R. D. Petrasso, and D. T. Casey, Phys. Plasmas **21**, 056315 (2014).

13. P. Michel *et al.*, Phys. Plasmas **16**, 042702 (2009).

14. I. V. Igumenshchev, W. Seka, D. H. Edgell, D. T. Michel, D. H. Froula, V. N. Goncharov, R. S. Craxton, L. Divol, R. Epstein, R. Follett, J. H. Kelly, T. Z. Kosc, A. V. Maximov, R. L. McCrory, D. D. Meyerhofer, P. Michel, J. F. Myatt, T. C. Sangster, A. Shvydky, S. Skupsky, and C. Stoeckl, Phys. Plasmas **19**, 056314 (2012).

15. M. L. Spaeth *et al.*, Fusion Sci. Technol. **69**, 25 (2016).

16. S. Skupsky, J. A. Marozas, R. S. Craxton, R. Betti, T. J. B. Collins, J. A. Delettrez, V. N. Goncharov, P. W. McKenty, P. B. Radha, T. R. Boehly, J. P. Knauer, F. J. Marshall, D. R. Harding, J. D. Kilkenny, D. D. Meyerhofer, T. C. Sangster, and R. L. McCrory, Phys. Plasmas **11**, 2763 (2004).

17. J. A. Marozas, F. J. Marshall, R. S. Craxton, I. V. Igumenshchev, S. Skupsky, M. J. Bonino, T. J. B. Collins, R. Epstein, V. Yu. Glebov, D. Jacobs-Perkins, J. P. Knauer, R. L. McCrory, P. W. McKenty, D. D.

Meyerhofer, S. G. Noyes, P. B. Radha, T. C. Sangster, W. Seka, and V. A. Smalyuk, Phys. Plasmas **13**, 056311 (2006).

18. J. A. Marozas, T. J. B. Collins, D. H. Edgell, I. V. Igumenshchev, and J. F. Myatt, Bull. Am. Phys. Soc. **56**, 241 (2011).

19. Concept initially presented by J. A. Marozas, T. J. B. Collins, J. D. Zuegel, P. B. Radha, F. J. Marshall, and W. Seka, presented at the 44th Annual Anomalous Absorption Conference, Estes Park, CO, 8–13 June 2014.

20. J. A. Marozas, T. J. B. Collins, J. D. Zuegel, P. W. McKenty, D. Cao, S. Fochs, and P. B. Radha, J. Phys.: Conf. Ser. **717**, 012107 (2016).

21. Inspired by Anishinaabe word *Adaawam*, meaning "to borrow something from someone," to describe the cross-beam energy transfer (CBET), just as energy is borrowed from one beam to another. Resource: J. D. Nichols and E. Nyholm, *A Concise Dictionary of Minnesota Ojibwe* (University of Minnesota, Minneapolis, 1995).

22. Inspired by Anishinaabe word *Mazinisin*, meaning "be imprinted, have a design," to describe laser energy deposition just as the laser imprints on and changes target morphology. Resource: J. D. Nichols and E. Nyholm, *A Concise Dictionary of Minnesota Ojibwe* (University of Minnesota, Minneapolis, 1995).

23. S. X. Hu, D. T. Michel, A. K. Davis, R. Betti, P. B. Radha, E. M. Campbell, D. H. Froula, and C. Stoeckl, Phys. Plasmas **23**, 102701 (2016).

24. T. P. Gill, *The Doppler Effect: An Introduction to the Theory of the Effect* (Logos, London, 1965).

25. J. J. MacFarlane *et al.*, High Energy Density Phys. **3**, 181 (2007).